

Electron tomography and holography in materials science

Paul A. Midgley^{1*} and Rafal E. Dunin-Borkowski^{2*}

The rapid development of electron tomography, in particular the introduction of novel tomographic imaging modes, has led to the visualization and analysis of three-dimensional structural and chemical information from materials at the nanometre level. In addition, the phase information revealed in electron holograms allows electrostatic and magnetic potentials to be mapped quantitatively with high spatial resolution and, when combined with tomography, in three dimensions. Here we present an overview of the techniques of electron tomography and electron holography and demonstrate their capabilities with the aid of case studies that span materials science and the interface between the physical sciences and the life sciences.

Over the past few years, transmission electron microscopy (TEM) has been revolutionized, not only by the introduction of new hardware such as field-emission electron guns, aberration correctors and monochromators, which are described elsewhere in this Insight edition^{1,2}, but also by the development of new techniques, algorithms and software that take advantage of increased computational speed and the ability to control and automate modern electron microscopes. Two techniques that have benefited from the introduction of digital image acquisition and the ability to record images under different electron optical or specimen conditions are electron tomography and electron holography. Electron tomography has been adopted rapidly by materials scientists as an important microscopy tool for the three-dimensional (3D) study of the morphologies and chemical compositions of nanostructures, and electron holography offers unique insights into the magnetic and electrostatic properties of materials. For each technique, multiple images must be acquired to reveal quantitative 3D, magnetic or electrical information, in combination with automation and analysis software, resulting in the need for challenging and often lengthy experiments.

Electron tomography

Although many forms of microscopy can be used to provide remarkable images of materials across a range of length scales, the majority of these techniques are used to record two-dimensional (2D) projections of 3D structures. However, the complexity of both natural and artificial materials, such as device architectures in modern integrated circuits, highlights the need to develop tools and techniques to explore the morphologies, compositions and physical properties of materials in three dimensions. Such 3D imaging techniques are encompassed by the field of tomography, which originates in a 1917 paper on the projection of an object into a lower-dimensional space³. Nearly 50 years later, tomographic X-ray scanning for 3D medical imaging was proposed⁴. These ideas were picked up by staff at EMI, who built the first X-ray computed tomography scanner in 1971 (ref. 5). (It is often claimed that EMI were able to fund work on the computed tomography project only because of the enormous revenue generated by sales of the Beatles records in the 1960s.) Since then the use and type of tomographic scanners for medical imaging has proliferated.

The first examples of 3D reconstructions using TEM were published in 1968 in three seminal papers. The first paper described the determination of the structure of a biological macromolecule — the helical symmetry of which allowed reconstruction from a single

projection⁶. The second paper showed how asymmetrical objects can be reconstructed from a sufficient number of projections⁷. The third paper demonstrated how the signal-to-noise ratio could be improved by using an average re-projection calculated from a tilt series of images⁸. Three methods evolved: (1) electron crystallography, in which diffraction patterns and/or high-resolution images are recorded from biological systems, such as proteins, for which crystals can be grown⁹; (2) single-particle analysis, in which images of the same ‘particle’ (for example a virus) are recorded at different, often random, orientations¹⁰; (3) electron tomography, in which images of a single object are recorded about a tilt axis¹¹.

Although electron tomography was first applied in materials science in the late 1980s, its popularity has increased only in the last decade, with the introduction of novel tomographic imaging modes, automation of microscope control, new reconstruction algorithms and the increased speed and ease of the computation involved. It is worth recalling, however, that electron tomography is not the only 3D imaging mode available to the materials scientist. X-ray tomography is a routine tool in many laboratories, with desktop instruments achieving a 3D resolution of a few micrometres. By using a synchrotron source, X-ray tomograms can be produced with sub-100-nm resolution, and a 2D spatial resolution of ~15 nm is possible using zone plates¹². An X-ray approach based on ‘diffractive imaging’, which involves recording a tilt series of coherent diffraction patterns and using phase-retrieval methods to reconstruct real-space tomograms, allows a transverse resolution of ~10 nm to be achieved¹³. Scanning probe microscopy has been used by recording images of fresh surfaces revealed sequentially using a calibrated chemical etch¹⁴. Atom probe tomography offers, in principle, atomic resolution in three dimensions¹⁵. Although recent developments have allowed problems with sample preparation and suitability to be overcome by using focused-ion-beam milling and laser-assisted field ionization, interpretation and the presence of artefacts remain a challenge.

The scanning electron microscope also provides an excellent platform for 3D imaging at the ‘mesoscale’ (20 nm to 20 μm)¹⁶. To achieve 3D imaging, new surfaces must be exposed in a sequential and controlled fashion. Modern ‘dual-beam’ instruments, which have both electron optical and ion optical columns, enable a focused gallium ion beam to mill thin slices sequentially and the electron beam to image each exposed surface using secondary or backscattered electrons. The in-plane resolution (typically ~5 nm) is finer than the slice thickness (typically ~100 nm), so the 3D resolution function is

¹Department of Materials Science & Metallurgy, University of Cambridge, Pembroke Street, Cambridge CB2 3QZ, UK. ²Center for Electron Nanoscopy, Technical University of Denmark, DK-2800 Kongens Lyngby, Denmark. *e-mail: pam33@cam.ac.uk; rdb@cen.dtu.dk.

highly anisotropic. As the generation of characteristic X-rays by the electron beam allows elemental maps to be recorded in most scanning electron microscopes, 3D compositional information can be obtained by recording sequential elemental maps¹⁷. Crystallographic information can also be retrieved from electron-backscattered diffraction patterns and a full 3D crystallographic analysis made from a volume of $\sim 50^3 \mu\text{m}^3$ in 24 h (refs 18,19).

Nanoscale tomography in TEM

For high-resolution ($\sim 1^3 \text{nm}^3$) 3D tomographic imaging in TEM, images are recorded every one or two degrees about a tilt axis, over as large a specimen tilt range as possible (Fig. 1a). Typically, the ensemble of images is then ‘back-projected’ to form a 3D reconstruction. The information required, and the type of specimen examined, often dictate which of the many imaging modes available in the TEM is used.

It is important to understand the limitations of tomography in TEM and the artefacts that may arise. Early examples of electron tomography in materials science used bright-field techniques and approaches based on work in the biological sciences to study stained polymer sections and the internal networks of block copolymers²⁰. Similarly, bright-field TEM was used to investigate the porosities of zeolitic materials²¹. In biological work and in non-crystalline inorganic systems, the use of bright-field TEM is possible because mass-thickness contrast satisfies the ‘projection requirement’ that the recorded signal should be a monotonic function of some physical property²². If this requirement is not satisfied, then reconstruction becomes complicated and conventional real-space back-projection may fail.

In general, the resolution of a reconstructed tomogram is governed by the number of images in the tilt series and by the tilt range over which the series is recorded. In simple terms, the (Crowther) resolution is equal to the angular increment of the tilt series multiplied by the size of the object²³. Thus, as well as needing a fine angular increment, the resolution scales with the size of the object studied. In practice, to limit beam damage and to keep acquisition times to a sensible level, images are recorded every 1–2°. With accurate, often iterative, reconstruction techniques, the resolution is then approximately 1/100 of the object diameter. Although real-space back-projection methods are used routinely for tomographic reconstruction, it is useful to consider that each projection corresponds to a central slice in Fourier space. By recording a tilt series about a single axis, low-frequency information is sampled more finely than higher frequency information. Thus, a simple back-projection, in which all of the information from the ensemble of images is smeared into 3D reconstruction space, leads to a blurred version of the original object. Two schemes exist to overcome this blurring. The first is to use a ramp-like weighting filter in Fourier space to enhance

the higher frequencies, suitably apodized to avoid enhancing noise²⁴. The second is an iterative scheme in which a reconstruction is re-projected along the original tilt series directions for comparison with the original recorded images²⁵. A difference image is formed at each of the tilt increments and a difference tomogram subsequently used to improve the reconstruction. An iterative procedure follows until no further improvement is seen, typically after 20–40 iterations. This iterative approach is one of a number of techniques that can be used to constrain the reconstruction to best fit the information available. By imposing constraints, the number of images required to achieve a high-fidelity reconstruction can be reduced considerably. This is the basis of ‘discrete tomography’. One implementation of this is the DART algorithm, which builds on the iterative reconstruction approach but adds extra constraints at each iteration²⁶. Specifically, the algorithm is told how many densities (or grey levels) should be present in the reconstruction. Often this prior information is known. In the extreme limit, only one density may be present in the object, so a binary solution is found—in this limit, if the signal-to-noise ratio is good then a handful of images may be enough to produce a high-fidelity reconstruction even for complex concave and convex structures²⁷.

When using conventional TEM samples and specimen holders, a tilt may be reached beyond which the sample is too thick or shadowing occurs owing to the holder, grid or other parts of the specimen. This tilt maximum leads to a ‘missing wedge’ of information, as shown in Fig. 1b. Such missing information can lead to artefacts, and reconstructions can be elongated in the direction of the missing wedge. The tilt range should therefore be as high as possible. Recent work has suggested that 75–80° should be sufficient to reduce artefacts to a minimum and not lead to serious errors when measuring object sizes or shapes²⁸. An alternative way of reducing the missing wedge is to record a second tilt series about an axis perpendicular to the first—a ‘dual-axis’ series. In practice, the sample is usually rotated by 90° and a second tilt series recorded. This approach can lead to a large improvement in the fidelity of the reconstruction²⁹, as seen in Fig. 2. There, dual-axis tomography has been combined with iterative reconstruction to constrain the reconstruction to best fit the images in both tilt series³⁰. For samples for which high tilts lead to large projected thicknesses, recording a dual-axis series with a smaller maximum tilt may be a better solution; for example, the fraction of missing information present in a dual-axis series recorded with $\pm 50^\circ$ tilt ($\sim 20\%$) is approximately the same as that recorded in a single tilt series with $\pm 70^\circ$ tilt. Ultrahigh-tilt holders are now commercially available, including those in which the use of a needle-shaped sample allows 360° rotation within the pole-piece gap of the objective lens, eliminating missing-wedge artefacts. Such specimens can be fabricated using a focused ion beam³¹. Indeed, similar tips are fabricated for atom probe tomography

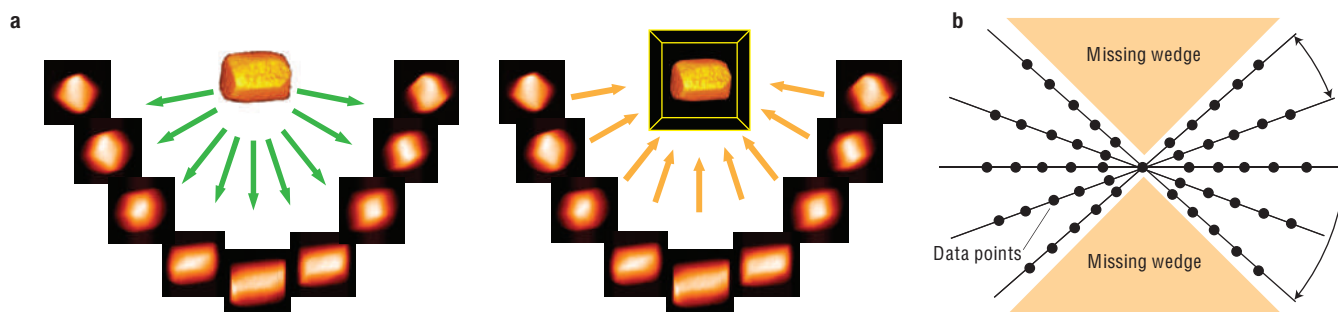


Figure 1 | Electron tomography. **a**, Illustration of two-stage tomography process with (left) acquisition of an ensemble of images (projections) about a single tilt axis and (right) the back-projection of these images into 3D object space. **b**, Representation in Fourier space of the ensemble of projections, indicating the undersampling of high-spatial-frequency information and the missing wedge of information brought about by a restricted tilt range. $\Delta\theta$ is the tilt increment between successive images and θ_{max} is the maximum tilt angle. (Adapted from ref. 29.)

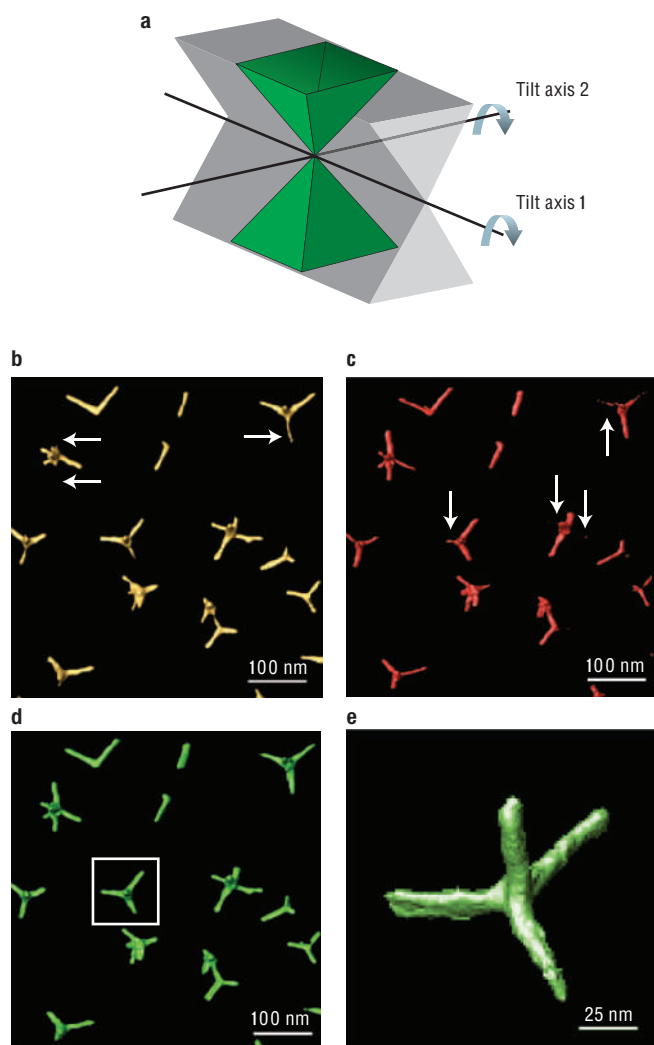


Figure 2 | Dual-axis electron tomography. **a**, Illustration showing how a dual-axis tilt series collapses a missing wedge into a missing pyramid of information. **b, c, d, e**, Reconstructions of cadmium telluride tetrapods from a dual-axis tilt series, reconstructed individually (**b, c**) and then as a dual-axis series (**d**). The tetrapod shown boxed in **d** is magnified in **e**. The arrows indicate regions where the missing wedge has had its greatest effect on the individual reconstructions. Each 'leg' of each tetrapod is better reconstructed in the dual-axis reconstruction. (Adapted from ref. 29.)

and the same tip can be imaged using both techniques, to provide complementary information³².

The TEM is a remarkably versatile instrument, and the strong interaction of the electron beam with the specimen leads to a host of possible imaging modes that can be used, in principle, for electron tomography. Bright-field TEM, which is used so prevalently in biological tomography, is not in general suited to the study of crystalline materials. Diffraction contrast and Fresnel fringes do not satisfy the projection requirement and can lead to serious artefacts in reconstructions. The image signal seen in the scanning TEM (STEM), using high-angle annular dark-field (HAADF) imaging, offers an excellent alternative. As described elsewhere in this Insight edition¹, STEM HAADF imaging can be considered incoherent, almost completely eliminating diffraction and phase contrast. The contrast is then, to a good approximation, monotonic with thickness, and is also sensitive to changes in composition; for a typical geometry and material, it is approximately proportional to $Z^{1.8}$, where Z is the

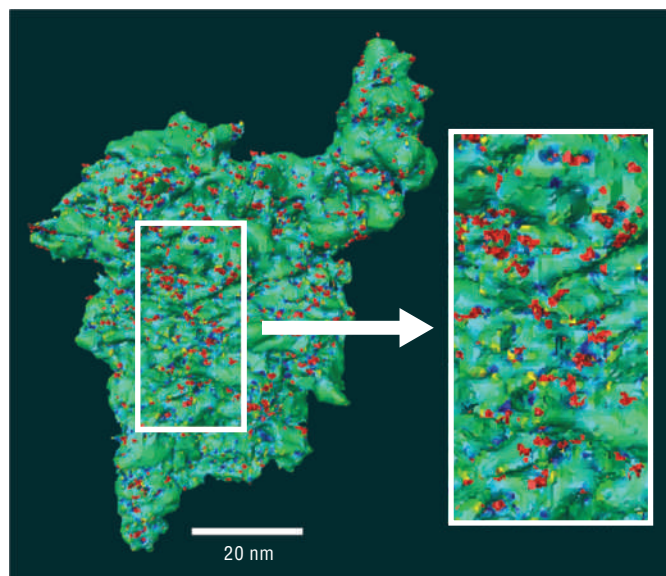


Figure 3 | Tomographic reconstruction of a heterogeneous catalyst. Surface-rendered representation of a tomographic reconstruction of a heterogeneous catalyst based on disordered mesoporous silica supporting bimetallic ruthenium–platinum nanoparticles. The surface has been colour-coded according to the Gaussian curvature of the surface, with blue regions delineating saddle points. The nanoparticles (red) appear to prefer to anchor themselves at the (blue) saddle points.

atomic number. These properties make the STEM HAADF signal ideal for tomographic applications³³. The earliest example of STEM HAADF tomography was in the study of heterogeneous catalysts based on metallic nanoparticles distributed within highly porous siliceous and carbonaceous support structures³⁴. There the STEM HAADF signal was able to discriminate nanometre-sized particles from the background support, whereas in bright-field TEM the contrast from the particles was very weak³⁵. More recent work³⁶ on similar catalyst structures, as shown in Fig. 3, has revealed the distribution of particles on and within a porous framework and the fractal nature of the internal surface. Theoretical work has shown that when two parallel chemical reactions are taking place on a fractal surface, the slower, often undesired, reaction can be suppressed. Figure 3 also shows that STEM tomography can be used to relate the distribution of particles to the underlying surface curvature, showing in this case the strong preference of the particles (red) for saddle-shaped anchor points (blue).

The suppression of unwanted diffraction contrast in STEM HAADF tomography has led to the study of faceting and crystal morphology. Figure 4 reveals the faceting of magnetite crystals that make up the 'backbone' of one strain of magnetotactic bacteria^{37,38}. Similar studies have now been completed on a number of nanocrystals, especially in catalyst systems where different facets can have different catalytic properties. STEM tomography has also been used to determine the real-space crystallography of mesoporous structures³⁹. For example, in MCM-48 mesoporous silica, which has a double-gyroid form, electron diffraction and 2D high-resolution electron microscopy (HREM) studies had concluded that an additional pore system was present in the system. STEM tomography was able to visualize this directly in three dimensions and confirm the space group symmetry⁴⁰.

In metallurgy, STEM tomography is especially useful for investigating the morphologies and distributions of precipitates in steels and alloys. Figure 5a shows an example of a surface-rendered reconstruction of germanium precipitates in an aluminium–germanium

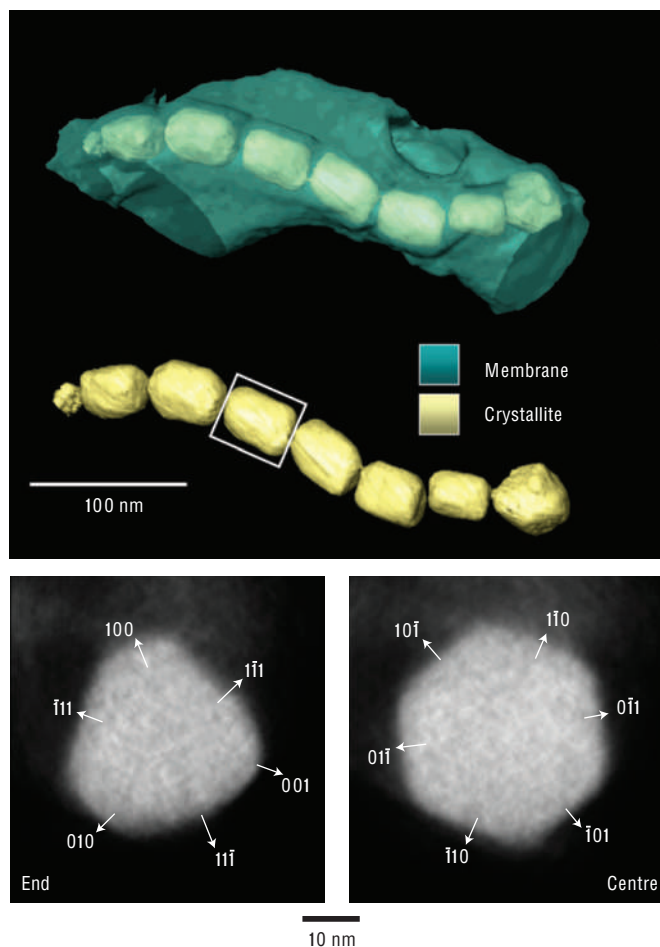


Figure 4 | Tomographic reconstruction of biogenic magnetite crystals. Tomographic reconstruction of a magnetotactic bacterium (strain MV-1) showing the internal backbone of magnetite crystals and the outer bacterial membrane. Slices taken from the end and centre of the boxed magnetite crystal, and perpendicular to the axis of the backbone, are shown in the lower part of the figure, illustrating the crystallography of the magnetite particles and the fidelity of the reconstruction. (Adapted from ref. 37).

alloy⁴¹. The different shapes revealed by the reconstruction have been colour-coded and the dotted lines delineate the traces of {111} planes in the aluminium-rich matrix. STEM tomography has been applied to structures at the interface of materials science and life science, such as carbon nanotubes in mammalian macrophages⁴² and the self-assembly of ferritin in liver cells⁴³. It has also been used (in conjunction with the DART algorithm mentioned previously) to investigate the morphologies of catalyst particles in multiwalled nanotubes⁴⁴ and has been adopted by the semiconductor industry to investigate faults and voids in device structures and to determine the shapes of metal interconnects⁴⁵.

For very thick samples and those with high mass density, STEM HAADF imaging is no longer suitable for tomographic applications as the signal may decrease as the sample thickness increases, because proportionately more scattering occurs outside the outer edge of the annular detector. Schemes have been proposed that use incoherent bright-field imaging to overcome this problem⁴⁶. In crystalline samples, STEM HAADF images are also affected by channelling. At major zone axes, the STEM probe may propagate preferentially down atom cores, leading to stronger scattering to large angles than at 'random' orientations. In the tilt series, such

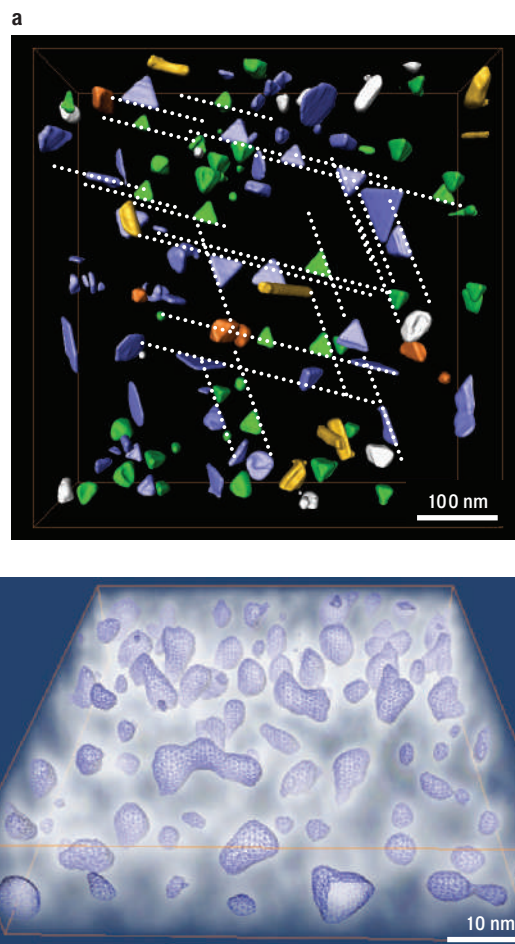


Figure 5 | 3D reconstructions of precipitates and nanoparticles.

a, Reconstruction obtained using STEM tomography of the distribution and morphology of germanium precipitates in an aluminium–germanium alloy. The colours differentiate the precipitate morphology: blue, platelets; green, tetrahedra; orange, octahedra; yellow, rods; white, irregular shapes. The dotted lines indicate traces of {111} planes. (Adapted from ref. 41.) **b**, Plasmon tomography of irregularly shaped silicon nanoparticles within a silica matrix. The white 'fog' is the reconstructed plasmon signal at 17 eV. (Reprinted from ref. 52).

axes can sometime be avoided, and/or overly bright images can be removed from the series without significant loss of tomographic resolution or fidelity.

In STEM tomography, compositional information is determined indirectly through the *Z* dependence of the signal. However, inelastic signals, such as those detected using electron energy-loss spectroscopy (EELS) and energy-dispersive X-ray spectroscopy (EDX), can be used to map composition in two dimensions and, by extension, in three dimensions. Energy-loss information can be recorded pixel by pixel as a sequence of spectra ('spectrum imaging'⁴⁷) or by choosing a particular energy loss (or a small width about that loss, typically 5–10 eV) and forming an image using electrons that have lost only those energies. The latter approach, known as energy-filtered TEM (EFTEM), can be extended to record images over an energy-loss series, which by analogy with the EELS method is called image spectroscopy^{48,49} or EFTEM spectrum imaging. By choosing a particular energy loss, elemental maps can be recorded over a tilt series. Examples of this approach have used plasmon losses⁵⁰ and core losses⁵¹, the latter being less prone to diffraction contrast but having a weaker signal. 3D compositional information can be extracted

from such EFTEM series, as illustrated in Fig. 5b⁵². More recently, image spectroscopy was extended to volume spectroscopy by recording a large energy series at every tilt angle⁵³. A low-loss series of a nanocomposite composed of a multiwalled carbon nanotube encased in nylon was recorded every 3 eV over a wide range of tilts. The different plasmon excitation energies of the nylon (~22 eV) and the nanotube (~27 eV) enabled the two components of the composite to be distinguished. By reconstructing tomograms at individual energy losses, it was possible to identify a voxel or subvolume common to all of the energy-loss tomograms and, by plotting the intensity of the voxel as a function of energy loss, to extract spectral information from within the tomogram. In conventional EELS, spectral information is always projected through the structure, but now it is possible to extract spectral information from a subvolume without any projection artefact.

Early attempts to map chemical information using EDX were complicated by the directionality and inefficiency of the sample-detector geometry, by the need to tilt away from the detector and by the consequent shadowing in half of the tilt series⁵⁴. Recent work has taken advantage of needle specimens, where shadowing is eliminated and the detector geometry is not such a problem⁵⁵. EELS, EFTEM and EDX images are all prone to diffraction effects through the coupling of elastic and inelastic signals. These can be minimized by forming jump-ratio images or dividing elemental maps by low-loss (or zero-loss) images. However, care must be taken if such images are used for tomography as the resultant signal may not satisfy the projection requirement.

Electron tomography has also been developed to study crystal-line defects, and especially dislocation networks, in three dimensions. By recording a tilt series of weak-beam dark-field images, it was possible to reveal a dislocation network in a gallium nitride epitaxial layer⁵⁶. However, to do so it is critical that the diffraction conditions do not change significantly as the tilt series is recorded (a difficult practical task) and that extraneous contrast, such as thickness fringe contrast, is minimized. Weak-beam dark-field tomography has also been used to investigate secondary phases in metallic alloys where ordered phases grow from the matrix. In conjunction with EFTEM tomography, the shapes and compositions of γ precipitates were determined in a nickel–aluminium–titanium superalloy⁵⁷. The practical difficulties of weak-beam dark-field tomography led to the development of a STEM analogue using a low-angle annular dark-field imaging mode in which a number of dark-field beams contribute to the image. The advantages of this method for dislocation tomography are that the image is less sensitive to changes in diffraction conditions, the image is effectively a sum of many dark-field images, which tends to average out thickness contrast but enhance (albeit slightly blur) dislocation contrast, and data collection is easily automated⁵⁸.

As well as being able to map morphology and composition, it is also possible to map physical properties in three dimensions using a combination of electron holography, which is sensitive to changes in electrostatic potentials and magnetic fields, and electron tomography. Such 3D potential and field mapping will be discussed below. A future goal is to be able to visualize atoms in three dimensions. True atomic-resolution tomography may become possible either using new aberration-corrected instruments^{59,60} in combination with the discrete constraint that the object is composed of atoms, or by using an aberration-corrected STEM to reduce the depth of field and recording a series of 'confocal' images to build up a 3D atomic lattice. Suggestions have been made to combine the confocal approach with a limited tilt series and use iterative constraints and discrete tomography algorithms to build up a best-fit 3D lattice. Electron diffractive imaging⁶¹, analogous to the synchrotron X-ray technique, may also be able to help in the quest for 3D lattice imaging.

Electron holography

Electron holography⁶² was originally proposed⁶³ as a means of correcting for electron microscope lens aberrations, substantially before the advent of the laser and the use of holography in light optics. The technique is based on the formation of an interference pattern or 'hologram' in the TEM. Its development followed from earlier experiments in electron interferometry^{64–66}, many of which took place at the University of Tübingen, and relied on the development and availability of high-brightness electron sources. The technique overcomes the important limitation of most TEM imaging modes, namely that only spatial distributions of image intensity are recorded. All information about the phase shift of the high-energy electron wave that passes through the specimen is then lost.

By contrast, electron holography allows the phase shift of the electron wave to be recovered. As the phase shift is sensitive to local variations in magnetic and electrostatic potential, the technique can be used to obtain quantitative information about magnetic and electric fields in materials and devices with a spatial resolution that can approach the nanometre scale. This capability is of great importance for the study of a wide variety of material properties, such as the characterization of magnetic domain walls in spintronic devices⁶⁷ and the factors that affect the coercive fields of individual magnetic nanostructures⁶⁸.

The original work⁶³ described the reconstruction of an image by illuminating an 'in-line' electron hologram with a parallel beam of light and using a spherical-aberration-correcting plate and an astigmatism corrector, but the image reconstructed in this way is disturbed by a 'ghost' or 'conjugate' twin image. The mode of electron holography that is most often used for tackling problems in materials science is instead the off-axis, or 'sideband', mode, which is available on many modern electron microscopes and has been applied to the characterization of materials as diverse as quantum well structures, magnetoresistive films, nanowires and semiconductor devices⁶⁹.

The electron microscope geometry for the TEM mode of off-axis electron holography is shown schematically in Fig. 6a. A field-emission electron gun is used to provide a highly coherent source of electrons. In reality, the source is never perfectly coherent, but the degree of coherence must be such that an interference fringe pattern of sufficient quality can be recorded within a reasonable acquisition time, during which specimen and/or beam drift must be negligible. Although electron holograms have historically been recorded on photographic film, digital acquisition using charge-coupled-device cameras is now common practice. To acquire an off-axis electron hologram, the specimen is positioned so that it covers approximately half the field of view. A voltage is then applied to an electrostatic 'biprism'⁷⁰, which is usually located in place of one of the conventional selected-area apertures in the microscope. The biprism is analogous to a glass prism in light optics, but takes the form of a fine (<1- μm diameter) wire that is often made from gold-coated quartz. The voltage applied to the biprism acts to tilt a 'reference' electron wave that passes through vacuum with respect to the electron wave that passes through the specimen. The two waves are allowed to overlap and interfere. If the electron source is sufficiently coherent then, in addition to a bright-field image of the specimen, an interference fringe pattern is formed on the detector in the overlap region. Just as in a textbook 'double-slit experiment', electrons are emitted one by one from the field-emission electron gun in the microscope. After being deflected by the biprism, they reach the detector and are detected individually as particles. When a large number of electrons has accumulated, their wave-like properties become apparent and an interference fringe pattern is built up.

The amplitude and the phase shift of the electron wave that leaves the specimen are recorded in the intensities and the positions of the interference fringes in the hologram, respectively. The phase shift is sensitive to the in-plane component of the

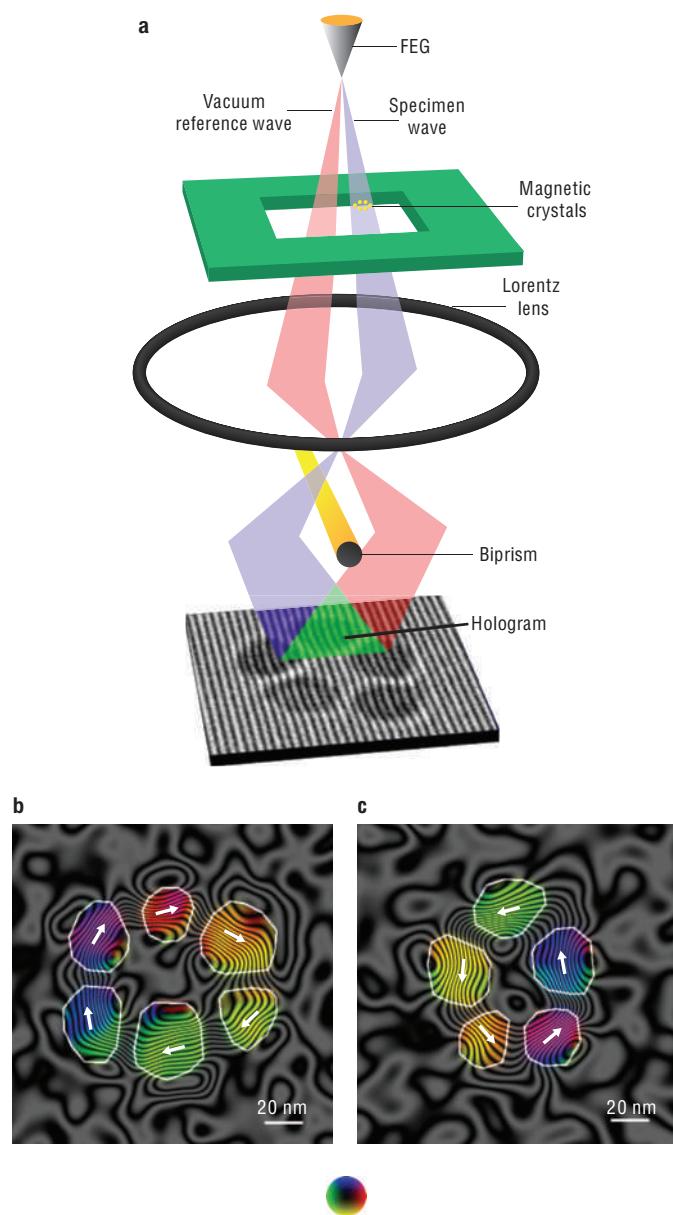


Figure 6 | Electron holography of magnetic nanoparticle rings.

a, Illustration of the application of a voltage to an electron biprism located close to a conjugate image plane in a field-emission electron gun (FEG) TEM, to overlap a vacuum reference electron wave with the electron wave that has passed through a region of the specimen to form an o -axis electron hologram. Variations in the spacing and direction of the recorded holographic interference fringes contain information about the projected magnetic flux density inside and surrounding the crystals. The experimental electron hologram shown in the figure was acquired from five 20-nm-diameter cobalt nanocrystals. The spacing of the holographic interference fringes is 3 nm.

b, c, Magnetic phase contours ($\times 128$ amplification; 0.049 rad spacing) formed from the magnetic contribution to the phase shift measured from two different cobalt nanoparticle rings. Each image was acquired with the specimen in magnetic-field-free conditions. The outlines of the nanoparticles are marked in white, and the direction of the measured magnetic induction is indicated using arrows and according to the colour wheel shown (red, right; yellow, down; green, left; blue, up). (Adapted from ref. 77.)

magnetic induction and the electrostatic potential in the specimen. Although the technique can be used to record phase information at atomic resolution (to improve the interpretable resolution

beyond the point resolution of the microscope)⁷¹ and to measure variations in specimen thickness and mean inner potential, here we concentrate on the ‘medium-resolution’ application of the technique to characterize longer-range electromagnetic fields. For studies of magnetic materials, a Lorentz lens (a high-strength mini-lens) allows the microscope to be operated at high magnification with the conventional objective lens switched off and the specimen either in magnetic-field-free conditions or in a chosen externally applied magnetic field. The typical field of view of such measurements is between a few hundred nanometres and a few micrometres, and the spatial resolution of the recorded electrostatic or magnetic fields can approach or exceed 5 nm.

Holography applications

The practical application of electron holography to the characterization of magnetic materials was pioneered by a research group at the Hitachi Advanced Research Laboratory in Japan⁷². Their work included studies of magnetic fields in fine particles, recorded media⁷³, flux vortices in superconductors^{74,75} and, most notably, the experimental verification of the Aharonov–Bohm effect and the confirmation of the physical reality of magnetic vector potentials⁷⁶. In each of these studies, the strength and direction of the local projected in-plane magnetic induction were obtained by displaying contours that had been generated from the magnetic contribution to the recorded electron holographic phase shift using a laser bench. A phase difference of 2π between any two contours corresponded to an enclosed magnetic flux of $4\pi \times 10^{-15}$ Wb. More recently, off-axis electron holography has been used to characterize magnetic states in nanostructures that are less than 100 nm in size⁷⁷. The application of electron holography to the study of magnetic nanocrystals of this size is challenging both because of a fundamental signal-to-noise limit and because the magnetic signal must be separated from unwanted contributions to the recorded phase shift from local variations in specimen thickness and composition. This separation can be achieved more reliably from electron holographic phase images than from images recorded using differential phase-contrast imaging in the STEM or the Fresnel or Foucault modes of Lorentz electron microscopy. Digital acquisition and analysis of electron holograms and sophisticated image analysis software are then essential.

Figure 6b and Fig. 6c illustrate the use of electron holography to image magnetostatic interactions between closely spaced nanoparticles of polycrystalline cobalt that each have diameters of ~ 20 nm. A ring of six cobalt particles has a diameter of less than 100 nm, with the constituent crystals each acting as single-domain magnets at room temperature. Such nanoscale rings are of interest for magnetic recording and storage applications because they can support bistable flux-closed magnetic states. Representative magnetic induction maps recorded using off-axis electron holography are shown in Fig. 6b, c in the form of phase contours, colours and arrows⁷⁸. The handedness of the magnetic domain structures in the rings is clear. A statistical sampling of magnetic states from such images indicates an approximately 50:50 mixture of clockwise and anticlockwise ground-state configurations, to which the rings relax after exposure to a saturating out-of-plane magnetic field. In each case, the magnetic induction is essentially confined within the annular ensemble.

Closely spaced magnetic nanocrystals that are found in nature are often more perfect in their sizes, shapes and arrangements than their synthetic counterparts. As a result, they can be used as model systems to study the effect of particle size, morphology, crystallography and spacing on magnetic microstructure. Figure 7a and Fig. 7b show chemical maps of a crystalline, naturally occurring magnetite–ulvöspinel (Fe_3O_4 – Fe_2TiO_4) mineral, which exsolved during slow cooling over geological timescales to yield an

intergrowth of ferrimagnetic magnetite-rich regions separated by non-magnetic ulvöspinel-rich lamellae. The remanent magnetization in such rocks is used by geophysicists to map the motions of continents and ocean beds resulting from the dynamics of plate tectonics. As an example of the application of electron holography to rock magnetism, Fig. 7c, d shows two remanent magnetic states recorded from the same region of the specimen. The induction maps show that individual 'blocks' of magnetite contain primarily single-domain magnetic states, which have lower energies than vortex states in the presence of strong interactions with neighbouring magnetic crystals^{79,80}. They also reveal the magnetostatic interaction fields between them. Magnetic superstates, in which clusters of magnetite blocks act collectively to form vortex and multidomain states that have zero net magnetization, are also visible. The images illustrate the complexity of the magnetic structure in this system. Electron holography has considerable potential for measuring both remanent magnetizations and magnetization reversal mechanisms in rocks, and for understanding mineral magnetism at the nanometre scale.

Similar magnetic interactions are observed in nature in magnetotactic bacteria, which contain single or multiple chains of ferrimagnetic magnetite (Fe_3O_4) or greigite (Fe_3S_4) crystals that are typically between 35 and 120 nm in size. In this size range, the crystals are uniformly magnetized single magnetic domains at room temperature. The arrangement of the crystals in linear chains results in a magnetic moment that orients the bacteria parallel to the geomagnetic field in an aquatic environment. A magnetic induction map recorded from a single helical bacterial cell containing a chain of equi-dimensional magnetite crystals is shown in Fig. 7e⁸¹. The magnetic phase contours are parallel to each other in the crystals and follow the chain axis. Unlike the more complicated magnetic arrangements seen in Fig. 7c, d, the magnetic moment in the linear bacterial chain is maximized, and its remanent magnetic state is almost equal to its saturated state. Although a single chain would appear to be ideal for magnetotaxis, a number of strains of bacteria possess either disorganized multiple arrangements of crystals⁸² or large crystals (up to 200 nm in length) that would each be expected to contain several magnetic domains if they were isolated.

For a fuller understanding of nanoparticle interactions and magnetic response, systematic studies of both continuous ferromagnetic films^{83,84} and lithographically patterned ferromagnetic nanostructures have been carried out using electron holography for different film thicknesses and element sizes, thicknesses and shapes, illustrating switching variability in nominally identical structures⁸⁵ and prompting consideration of modified shapes such as rings, slotted disks and slotted rings for applications⁸⁶.

The development of electron holography for the characterization of electrostatic fields in materials has a long history, most notably at the University of Bologna^{87,88}. Although it has been used to characterize the electric fields of microtips⁸⁹, electrically biased carbon nanotubes⁹⁰ and electroceramics, perhaps the most important potential application of electron holography in materials science and technology is the prospect that the technique can fulfil the requirement of the semiconductor industry to provide quantitative information about electrostatic potentials in doped semiconductors (and in ferroelectric materials⁹¹) with nanometre spatial resolution. Figure 8a illustrates the geometry of a semiconductor p–n junction in a thin TEM sample. The true junction potential (Fig. 8b) is assumed to lie within specimen thickness, t_{ej} , which is smaller than the total specimen thickness, t , as a result of the presence of specimen surfaces that are altered electrically as a result of the presence of surface states and specimen preparation for electron microscopy. A representative phase image recorded from a silicon p–n junction using electron holography is shown in Fig. 8c; p-type and n-type regions are delineated clearly as areas of darker and lighter contrast,

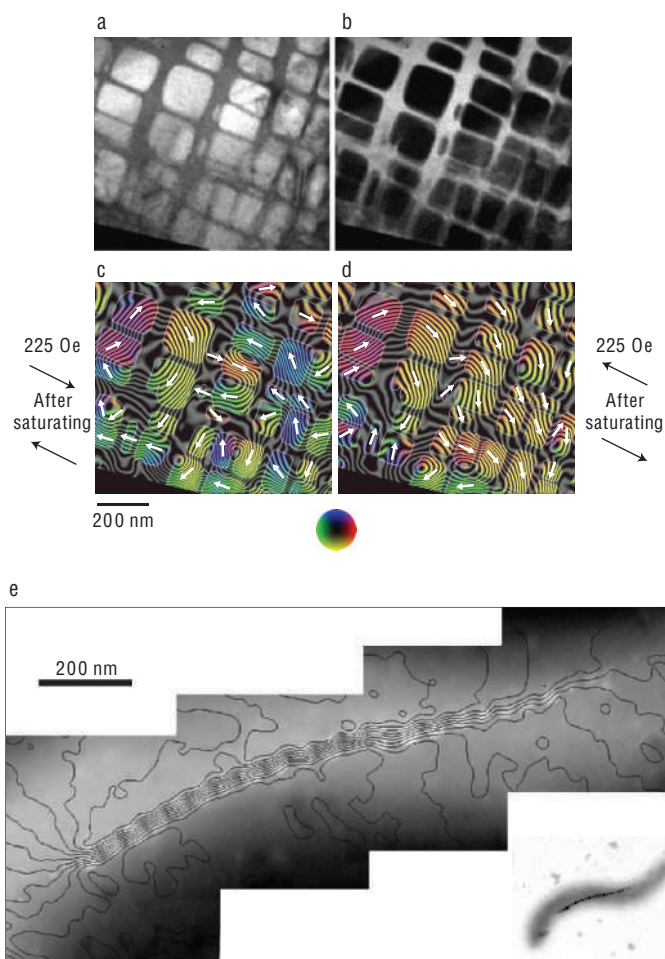


Figure 7 | Magnetic induction maps of geological and biogenic magnetic particles. **a, b**, Three-window background-subtracted elemental maps acquired from a naturally occurring titanomagnetite sample with a Gatan imaging filter using the iron L edge (**a**) and the titanium L edge (**b**). Brighter contrast indicates higher concentrations of iron and titanium in (**a**) and (**b**), respectively. **c, d**, Magnetic phase contours from the same region, measured using electron holography. Each image was acquired with the specimen in magnetic-field-free conditions. The outlines of magnetite-rich regions are marked in white, and the direction of the measured magnetic induction is indicated using arrows and according to the colour wheel shown (red, right; yellow, down; green, left; blue, up). The image in **c** was acquired after applying a large (>10,000 Oe) field towards the top left, then the indicated (225 Oe) field towards the bottom right, after which the external magnetic field was removed for hologram acquisition. The image in **d** was acquired after applying identical fields in the opposite directions. (Adapted from ref. 77.) **e**, Contours of 0.064-rad spacing formed from the magnetic contribution to the holographic phase shift acquired from a single bacterial cell (inset) of *Magnetospirillum magnetotacticum* strain MS-1, imaged in magnetic-field-free conditions. The contours, which spread out at the ends of the chain, are overlaid onto the contribution of the mean inner potential to the phase shift, to allow the positions of the crystals to be correlated with the magnetic contours. (Adapted from ref. 81.)

respectively. Similar phase images are now used routinely to characterize electrostatic potentials at source and drain regions in transistors^{92,93}, and techniques have been developed to measure electrostatic potentials in reverse-biased semiconductor devices prepared for TEM examination using focused-ion-beam milling⁹⁴. However, questions still remain about aspects of the interpretation of such

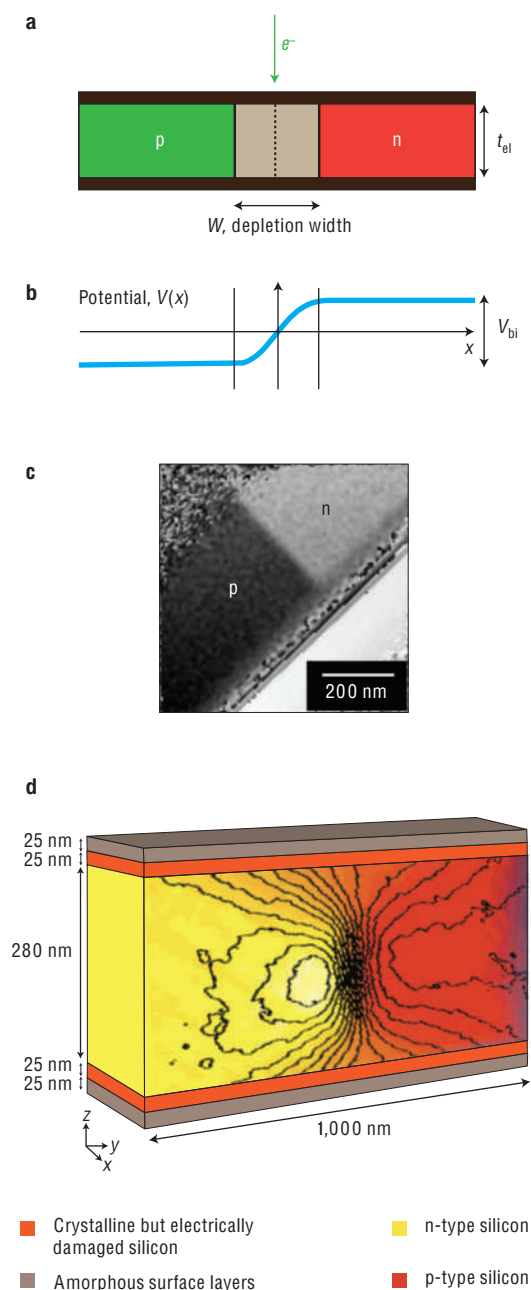


Figure 8 | Electron holographic tomography. **a**, Diagram showing the cross-sectional geometry of a TEM specimen of uniform thickness that contains a symmetrical semiconductor p–n junction. The thickness of the ‘electrically active’ specimen is denoted by t_{bi} . The layers at the top and bottom surfaces of the specimen represent electrically passivated or depleted layers, the physical and electrical nature of which is affected by TEM specimen preparation. **b**, Diagram showing the electrostatic potential profile across the p–n junction. The built-in voltage is denoted by V_{bi} and W is the width of the depletion region over which the potential changes. The sign convention for the potential is consistent with the mean inner potential of the specimen being positive relative to vacuum. **c**, Representative phase image reconstructed from an α -axis electron hologram of a silicon p–n junction sample. The sample edge is at the lower right of the image, and no attempt has been made to remove phase ‘wraps’ lying along this edge. The sign convention for the potential is as in **b**. **d**, Tomographic reconstruction of the electrostatic potential in a focused-ion-beam-milled specimen containing an electrically biased silicon p–n junction. Contours spaced every 0.2 V have been superimposed onto the reconstructed tomogram. (Adapted from refs 95 and 101.)

images^{95,96}, and approaches such as *in situ* annealing of specimens in the TEM⁹⁷ and simulations of the effect of the presence of the specimen surfaces⁹⁸ and the high-energy electron beam⁹⁹ on the electrical properties of the specimen are being studied. An interesting variant of off-axis electron holography, which can be used to provide 2D information about strain distributions in semiconductors, has recently been developed. This approach involves using the electrostatic biprism to form a dark-field electron hologram by interfering with each other diffracted electrons that have been scattered in strained and unstrained regions of the specimen¹⁰⁰.

Electron holographic tomography

A particularly exciting prospect is the combination of electron holography with electron tomography to characterize electrostatic and magnetic fields inside nanostructured materials with nanometre spatial resolution in three dimensions, rather than simply in projection, by acquiring ultrahigh-tilt series of electron holograms. Both the electrostatic phase shift and the magnetic phase gradient recorded using electron holography satisfy the projection requirement for electron tomographic reconstruction. Figure 8d shows the extremely promising result of an experiment performed to characterize the 3D electrostatic potential of a semiconductor p–n junction in a thin TEM specimen examined under an applied reverse bias, in which the effect of the surfaces of the thin specimen on the internal potential has been measured in three dimensions¹⁰¹. The prospect of characterizing magnetic vector fields inside nanocrystals in three dimensions by combining electron tomography with electron holography is also of great interest^{102,103}. This approach has previously been used to image magnetic fringing fields outside materials in three dimensions, by acquiring two ultrahigh-tilt series of differential phase-contrast images or electron holograms about orthogonal specimen tilt axes¹⁰⁴. Although the theory underlying such measurements is well established¹⁰⁵, their application to the characterization of magnetic fields inside nanostructured materials is complicated by the fact that the (often dominant) contribution of the mean inner potential to the measured phase shift must be removed at each sample tilt angle. Four tilt series of holograms may then be required. In addition, the need to acquire electron holograms at high specimen tilt angles about two axes imposes additional requirements on the specimen geometry.

Concluding remarks

Electron tomographic acquisition and reconstruction, coupled with the remarkably large number of imaging modes available in the electron microscope, ensures that a diversity of 3D structural and chemical information can be obtained from a variety of materials. There is great scope to develop the technique further as a reliable method for quantitative measurements of the physical and chemical properties of nanoscale structures in three dimensions, to move towards genuine 3D nanometrology. Off-axis electron holography provides quantitative information about electrostatic and magnetic fields in materials, as well as allowing fundamental studies of the physics of electromagnetic fields in nanoscale structures. Considerable further work is possible to develop, optimize and automate the technique, including the measurement of weak fields (towards detecting single magnetic spins), the development of approaches for improving its time resolution (for studying chemical reactions, biological samples and beam-sensitive materials such as zeolites) and overcoming the effects of specimen preparation and electron irradiation on measurements of electrostatic fields.

As well as individually providing unique high-spatial-resolution information, electron tomography and electron holography can be combined with other capabilities available in modern electron microscopes, including aberration-corrected imaging, *in situ* environmental cells and the ability to examine working devices

under applied bias or during mechanical deformation. Although the need to acquire multiple images still limits their application to truly dynamic studies, advances in both techniques are leading to the development of a true laboratory in the electron microscope.

References

- Muller, D. A. Structure and bonding at the atomic scale by scanning transmission electron microscopy. *Nature Mater.* **8**, 263–270 (2009).
- Urban, K. W. Is science prepared for atomic-resolution microscopy? *Nature Mater.* **8**, 260–262 (2009).
- Radon, J. Über die Bestimmung von Funktionen durch ihre Integralwerte langs gewisser Mannigfaltigkeiten. *Ber. Verh. K. Sachs. Ges. Wiss. Leipzig Math.-Phys. Kl.* **69**, 262–277 (1917).
- Cormack, A. M. Representation of a function by its line integrals with some radiological applications. *J. Appl. Phys.* **34**, 2722–2727 (1963).
- Hounsfield, G. N. A method of and apparatus for examination of a body by radiation such as X or gamma radiation. UK patent 1,283,915 (1972).
- De Rosier, D. J. & Klug, A. Reconstruction of three dimensional structures from electron micrographs. *Nature* **217**, 130–134 (1968).
- Hoppe, W., Langer, R., Knesch, G. & Poppe, C. Protein-kristallstrukturanalyse mit Elektronenstrahlen. *Naturwissenschaften* **55**, 333–336 (1968).
- Hart, R. G. Electron microscopy of unstained biological material: the polytropic montage. *Science* **159**, 1464–1467 (1968).
- Unwin, P. N. T. & Henderson, R. Molecular structure determination by electron microscopy of unstained crystalline specimens. *J. Mol. Biol.* **94**, 425–440 (1975).
- Frank, J. *Three-Dimensional Electron Microscopy of Macromolecular Assemblies* (Academic, 1996).
- Baumeister, W., Grimm, R. & Walz, J. Electron tomography of molecules and cells. *Trends Cell Biol.* **9**, 81–85 (1999).
- Chao, W., Hartneck, B. D., Liddle, J. A., Anderson, E. H. & Attwood, D. T. Soft X-ray microscopy at a spatial resolution better than 15nm. *Nature* **435**, 1210–1213 (2005).
- Chapman, H. N. et al. High-resolution ab initio three-dimensional X-ray diffraction microscopy. *J. Opt. Soc. Am. A* **23**, 1179–1200 (2006).
- Magerle, R. Nanotomography. *Phys. Rev. Lett.* **85**, 2749–2752 (2000).
- Cerezo, A., Godfrey, T. J. & Smith, G. D. W. Application of a position-sensitive detector to atom probe microanalysis. *Rev. Sci. Instrum.* **59**, 862–866 (1988).
- Inkson, B. J., Mulvihill, M. & Möbus, G. 3D determination of grain shape in a FeAl-based nanocomposite by 3D FIB tomography. *Scripta Mater.* **45**, 753–758 (2001).
- Schaffer, M., Wagner, J., Schaffer, B., Schmied, M. & Mulders, H. Automated three-dimensional X-ray analysis using a dual-beam FIB. *Ultramicroscopy* **107**, 587–597 (2007).
- Konrad, J., Zaefferer, S. & Raabe, D. Investigation of orientation gradients around a hard Laves particle in a warm-rolled Fe₃Al-based alloy using a 3D EBSD-FIB technique. *Acta Math.* **54**, 1369–1380 (2006).
- Uchic, M. D., Groeber, M. A., Dimiduk, D. M. & Simmons, J. P. 3D microstructural characterization of nickel superalloys via serial-sectioning using a dual beam FIB-SEM. *Scripta Mater.* **55**, 23–28 (2006).
- Spontak, R. J., Williams, M. C. & Agard, D. A. Three-dimensional study of cylindrical morphology in a styrene-butadiene-styrene block copolymer. *Polymer* **29**, 387–395 (1988).
- Koster, A. J., Ziese, U., Verkleij, A. J., Janssen, A. H. & de Jong, K. P. Three-dimensional electron microscopy: a novel imaging and characterization technique with nanometer scale resolution for materials science. *J. Phys. Chem. B* **104**, 9368–9370 (2000).
- Hawkes, P. W. *The Electron Microscope as a Structure Projector in Electron Tomography: Three-Dimensional Imaging with the Transmission Electron Microscope* (ed. Frank, J.) 17–39 (Plenum, 1992).
- Crowther, R. A., de Rosier, D. J. & Klug, A. The reconstruction of a three-dimensional structure from projections and its application to electron microscopy. *Proc. R. Soc. Lond. A* **319**, 317–340 (1970).
- Radermacher, M. *Weighted Back-Projection Methods in Electron Tomography* 2nd edn (ed. Frank, J.) 245–274 (Springer, 2006).
- Gilbert, P. Iterative methods for the three-dimensional reconstruction of an object from projections. *J. Theor. Biol.* **36**, 105–117 (1972).
- Batenburg, K. J. & Sijbers, J. in *Proc. IEEE Conf. Image Processing* Vol. 4, 133–136 (IEEE, 2007).
- Batenburg, K. J. *Network Flow Algorithms for Discrete Tomography*. Ph.D. thesis, Univ. Leiden; <http://visielab.ua.ac.be/staff/batenburg/papers/ba_phdthesis_2006.pdf> (2006).
- Kawase, N., Kato, M., Nishioka, H. & Jinnai, H. Transmission electron microtomography without the “missing wedge” for quantitative structural analysis. *Ultramicroscopy* **107**, 8–15 (2007).
- Arslan, I., Tong, J. R. & Midgley, P. A. Reducing the missing wedge: high-resolution dual axis tomography of inorganic materials. *Ultramicroscopy* **106**, 994–1000 (2006).
- Tong, J. R., Arslan, I. & Midgley, P. A. A novel dual-axis iterative algorithm for electron tomography. *J. Struct. Biol.* **153**, 55–63 (2006).
- Koguchi, M. et al. Three-dimensional STEM for observing nanostructures. *J. Electron Microsc. 50*, 235–241 (2001).
- Arslan, I., Marquis, E. A., Homer, M., Hekmaty, M. A. & Bartelt, N. C. Towards better 3-D reconstructions by combining electron tomography and atom-probe tomography. *Ultramicroscopy* **108**, 1579–1585 (2008).
- Midgley, P. A. & Weyland, M. 3D electron microscopy in the physical sciences: the development of Z-contrast and EFTEM tomography. *Ultramicroscopy* **96**, 413–431 (2003).
- Midgley, P. A., Weyland, M., Thomas, J. M. & Johnson, B. F. G. Z-Contrast tomography: a technique in three-dimensional nanostructural analysis based on Rutherford scattering. *Chem. Commun.* **10**, 907–908 (2001).
- Thomas, J. M. et al. The chemical application of high-resolution electron tomography: bright field or dark field? *Angew. Chem. Int. Ed.* **43**, 6745–6747 (2004).
- Ward, E. P. W., Yates, T. J. V., Fernández, J.-J., Vaughan, D. E. W. & Midgley, P. A. Three-dimensional nanoparticle distribution and local curvature of heterogeneous catalysts revealed by electron tomography. *J. Phys. Chem. C* **111**, 11501–11505 (2007).
- Weyland, M., Yates, T. J. V., Dunin-Borkowski, R. E., Laffont, L. & Midgley, P. A. Nanoscale analysis of three-dimensional structures by electron tomography. *Scripta Mater.* **55**, 29–33 (2006).
- Buseck, P. R. et al. Magnetite morphology and life on Mars. *Proc. Natl Acad. Sci. USA* **98**, 13490–13495 (2001).
- De Jong, K. P. & Koster, A. J. Three-dimensional electron microscopy of mesoporous materials - recent strides towards spatial imaging at the nanometer scale. *ChemPhysChem* **3**, 776–780 (2002).
- Yates, T. J. V. et al. Three-dimensional real-space crystallography of MCM-48 mesoporous silica revealed by scanning transmission electron tomography. *Chem. Phys. Lett.* **418**, 540–543 (2006).
- Kaneko, K. et al. TEM characterization of Ge precipitates in an Al-1.6 at% Ge alloy. *Ultramicroscopy* **108**, 210–220 (2008).
- Porter, A. E. et al. Direct imaging of single-walled carbon nanotubes in human cells. *Nature Nanotechnol.* **2**, 713–717 (2007).
- Midgley, P. A., Weyland, M. & Stegmann, H. in *Advanced Tomographic Methods in Materials Research and Engineering* (ed. Banhart, J.) 335–373 (Oxford Univ. Press, 2008).
- Bals, S., Batenburg, K. J., Verbeeck, J., Sijbers, J. & van Tendeloo, G. Quantitative three-dimensional reconstruction of catalyst particles for bamboo-like carbon nanotubes. *Nano Lett.* **7**, 3669–3674 (2007).
- Kubel, C. et al. Recent advances in electron tomography: TEM and HAADF-STEM tomography for materials science and semiconductor applications. *Microsc. Microanal.* **11**, 378–400 (2005).
- Ercius, P., Weyland, M., Muller, D. A. & Gignac, L. M. Three-dimensional imaging of nanovoids in copper interconnects using incoherent bright field tomography. *Appl. Phys. Lett.* **88**, 243116 (2006).
- Jeanguillaume, C. & Colliex, C. Spectrum-image: the next step in EELS digital acquisition and processing. *Ultramicroscopy* **28**, 252–257 (1989).
- Lavergne, J. L., Martin, J. M. & Belin, M. interactive electron-energy-loss elemental mapping by the imaging-spectrum method. *Microsc. Microanal. Microstruct.* **3**, 517–528 (1992).
- Thomas, P. J. & Midgley, P. A. Image-spectroscopy - I. The advantages of increased spectral information for compositional EFTEM analysis. *Ultramicroscopy* **88**, 179–186 (2001).
- Mobus, G. & Inkson, B. J. Three-dimensional reconstruction of buried nanoparticles by element-sensitive tomography based on inelastically scattered electrons. *Appl. Phys. Lett.* **79**, 1369–1371 (2001).
- Weyland, M. & Midgley, P. A. Extending energy-filtered transmission electron microscopy (EFTEM) into three dimensions using electron tomography. *Microsc. Microanal.* **9**, 542–555 (2003).
- Yurtsever, A., Weyland, M. & Muller, D. A. Three-dimensional imaging of nonspherical silicon nanoparticles embedded in silicon oxide by plasmon tomography. *Appl. Phys. Lett.* **89**, 151920 (2006).
- Gass, M. H., Koziol, K. K. K., Windle, A. H. & Midgley, P. A. 4-dimensional spectral-tomography of carbonaceous nano-composites. *Nano Lett.* **6**, 376–379 (2006).
- Mobus, G., Doole, R. C. & Inkson, B. J. Spectroscopic electron tomography. *Ultramicroscopy* **96**, 433–451 (2003).
- Yaguchi, T. et al. Elemental mapping using a dedicated FIB/STEM system. *Microsc. Microanal.* **10** (suppl. 2), 1030–1031 (2004).
- Barnard, J. S., Sharp, J., Tong, J. R. & Midgley, P. A. High-resolution three-dimensional imaging of dislocations. *Science* **303**, 319 (2006).
- Hata, S. et al. Electron tomography imaging and analysis of γ and γ' domains in Ni-based superalloys. *Adv. Mater.* **20**, 1905–1909 (2008).
- Sharp, J. H., Barnard, J. S., Kaneko, K., Higashida, K. & Midgley, P. A. Dislocation tomography made easy: a reconstruction from ADF STEM images obtained using automated image shift correction. *J. Phys. Conf. Ser.* **126**, 012013 (2008).

59. Sadan, M. B. *et al.* Toward atomic-scale bright-field electron tomography for the study of fullerene-like nanostructures. *Nano Lett.* **8**, 891–896 (2008).
60. Jinschek, J. R. *et al.* 3-D reconstruction of the atomic positions in a simulated gold nanocrystal based on discrete tomography: prospects of atomic resolution electron tomography. *Ultramicroscopy* **108**, 589–604 (2008).
61. Rodenburg, J. M., Hurst, A. C. & Cullis, A. G. Transmission microscopy without lenses for objects of unlimited size. *Ultramicroscopy* **107**, 227–231 (2007).
62. Midgley, P. A. An introduction to electron holography. *Micron* **32**, 167–184 (2001).
63. Gabor, D. Microscopy by reconstructed wavefronts. *Proc. R. Soc. Lond. A* **197**, 454–487 (1949).
64. Jönsson, C. Elektroneninterferenzen an mehreren künstlich hergestellten Feinspalten. *Z. Phys. A* **161**, 454–474 (1961).
65. Merli, P. G., Missiroli, G. F. & Pozzi, G. On the statistical aspect of electron interference phenomena. *Am. J. Phys.* **44**, 306–307 (1976).
66. Tonomura, A., Endo, J., Matsuda, T., Kawasaki, T. & Ezawa, H. Demonstration of single-electron build-up of an interference pattern. *Am. J. Phys.* **57**, 117–120 (1989).
67. Junginger, F. *et al.* Spin torque and heating effects in current-induced domain wall motion probed by high-resolution transmission electron microscopy. *Appl. Phys. Lett.* **90**, 132506 (2007).
68. Bromwich, T. J. *et al.* Remanent magnetic states and interactions in nanopillars. *Nanotechnology* **17**, 4367–4373 (2006).
69. Völkl, E., Allard, L. F. & Joy, D. C. (eds) *Introduction to Electron Holography* (Plenum, 1998).
70. Möllenstedt, G. & Düker, H. Fresnel'scher Interferenzversuch mit einem Biprisma für Elektronenwellen. *Naturwissenschaften* **42**, 41 (1955).
71. Orchowski, A., Rau, W. D. & Lichte, H. Electron holography surmounts resolution limit of electron microscopy. *Phys. Rev. Lett.* **74**, 399–402 (1995).
72. Tonomura, A. *Electron Holography* (Springer, 1999).
73. Osakabe, N. *et al.* Observation of recorded magnetization pattern by electron holography. *Appl. Phys. Lett.* **42**, 746–748 (1983).
74. Hasegawa, S. *et al.* Magnetic-flux quanta in superconducting thin films observed by electron holography and digital phase analysis. *Phys. Rev. B* **43**, 7631–7650 (1991).
75. Bonevich, J. E. *et al.* Electron holography observation of vortex lattices in a superconductor. *Phys. Rev. Lett.* **70**, 2952–2955 (1993).
76. Tonomura, A. *et al.* Evidence for Aharonov-Bohm effect with magnetic field completely shielded from electron wave. *Phys. Rev. Lett.* **56**, 792–795 (1986).
77. Dunin-Borkowski, R. E. *et al.* Off-axis electron holography of magnetic nanowires and chains, rings and planar arrays of magnetic nanoparticles. *Microsc. Res. Tech.* **64**, 390–402 (2004).
78. Tripp, S. L., Dunin-Borkowski, R. E. & Wei, A. Flux closure in self-assembled cobalt nanoparticle rings. *Angew. Chem.* **42**, 5591–5593 (2003).
79. Harrison, R. J., Dunin-Borkowski, R. E. & Putnis, A. Direct imaging of nanoscale magnetic interactions in minerals. *Proc. Natl Acad. Sci. USA* **99**, 16556–16561 (2002).
80. Feinberg, J. M. *et al.* Effects of internal mineral structures on the magnetic remanence of silicate-hosted titanomagnetite inclusions: an electron holography study. *J. Geophys. Res.* **111**, B12S15 (2006).
81. Dunin-Borkowski, R. E. *et al.* Magnetic microstructure of magnetotactic bacteria by electron holography. *Science* **282**, 1868–1870 (1998).
82. Kasama, T. *et al.* Magnetic properties, microstructure, composition and morphology of greigite nanocrystals in magnetotactic bacteria from electron holography and tomography. *Am. Mineral.* **91**, 1216–1229 (2006).
83. Loudon, J. C., Mathur, N. D. & Midgley, P. A. Charge-ordered ferromagnetic phase in $\text{La}_{0.5}\text{Ca}_{0.5}\text{MnO}_3$. *Nature* **420**, 797–800 (2002).
84. Murakami, Y., Yoo, J. H., Shindo, D., Atou, T. & Kikuchi, M. Magnetization distribution in the mixed-phase state of hole-doped manganites. *Nature* **423**, 965–968 (2003).
85. Kasama, T. *et al.* Off-axis electron holography of pseudo-spin-valve thin film magnetic elements. *J. Appl. Phys.* **98**, 013903 (2005).
86. Hu, H., Wang, H., McCartney, M. R. & Smith, D. J. Switching mechanisms and remanent states for nanoscale slotted Co circular elements studied by electron holography. *Phys. Rev. B* **73**, 153401 (2006).
87. Merli, P. G., Missiroli, G. F. & Pozzi, G. P-n junction observations by interference electron microscopy. *J. Microscopy* **21**, 11–20 (1974).
88. Frabboni, S., Matteucci, G. & Pozzi, G. Observation of electrostatic fields by electron holography: the case of reversed biased p-n junctions. *Ultramicroscopy* **23**, 29–38 (1987).
89. Matteucci, G., Missiroli, G. F., Muccini, M. & Pozzi, G. Electron holography in the study of the electrostatic fields: the case of charged microtips. *Ultramicroscopy* **45**, 77–83 (1992).
90. Cumings, J., Zettl, A., McCartney, M. R. & Spence, J. C. H. Electron holography of field-emitting carbon nanotubes. *Phys. Rev. Lett.* **88**, 056804 (2002).
91. Matsumoto, T. *et al.* Ferroelectric 90° domain structure in a thin film of BaTiO_3 fine ceramics observed by 300 kV electron holography. *Appl. Phys. Lett.* **92**, 072902 (2008).
92. Rau, W. D., Schwander, P., Baumann, F. H., Höppner, W. & Ourmazd, A. Two-dimensional mapping of the electrostatic potential in transistors by electron holography. *Phys. Rev. Lett.* **82**, 2614–2617 (1999).
93. Gribelyuk, M. A. *et al.* Mapping of electrostatic potential in deep submicron CMOS devices by electron holography. *Phys. Rev. Lett.* **89**, 025502 (2002).
94. Twitchett, A. C., Dunin-Borkowski, R. E. & Midgley, P. A. Quantitative electron holography of biased semiconductor devices. *Phys. Rev. Lett.* **88**, 238302 (2002).
95. Twitchett, A. C., Dunin-Borkowski, R. E., Hallifax, R. J., Broom, R. F. & Midgley, P. A. Off-axis electron holography of unbiased and reverse-biased focused ion beam milled Si p-n junctions. *Microsc. Microanal.* **11**, 66–78 (2005).
96. Cooper, D., Twitchett-Harrison, A. C., Midgley, P. A. & Dunin-Borkowski, R. E. The influence of electron irradiation on electron holography of focused ion beam milled GaAs p-n junctions. *J. Appl. Phys.* **101**, 094508 (2007).
97. Cooper, D. *et al.* Improvement in electron holographic phase images of focused-ion-beam-milled GaAs and Si p-n junctions by in situ annealing. *Appl. Phys. Lett.* **88**, 063510 (2006).
98. Beleggia, M., Fazzini, P. F., Merli, P. G. & Pozzi, G. Influence of charged oxide layers on TEM imaging of reverse-biased p-n junctions. *Phys. Rev. B* **67**, 045328 (2003).
99. Houben, L., Luysberg, M. & Brammer, T. Illumination effects in holographic imaging of the electrostatic potential in semiconductors in transmission electron microscopy. *Phys. Rev. B* **70**, 165313 (2004).
100. Hýtch, M. J., Houdellier, F., Hüe, F. & Snoeck, E. Nanoscale holographic interferometry for strain measurements in electronic devices. *Nature* **453**, 1086–1089 (2008).
101. Twitchett-Harrison, A. C., Yates, T. J. V., Newcomb, S. B., Dunin-Borkowski, R. E. & Midgley, P. A. High-resolution three-dimensional mapping of semiconductor dopant potentials. *Nano Lett.* **7**, 2020–2023 (2007).
102. Kasama, T., Antypas, Y., Chong, R. K. K. & Dunin-Borkowski, R. E. in *Electron Microscopy of Molecular and Atom-Scale Mechanical Behavior, Chemistry and Structure* (eds Martin, D. C., Muller, D. A., Midgley, P. A. & Stach, E. A.) P5.01 (*Mater. Res. Soc. Proc.* **839**, 2005).
103. Phatak, C., Beleggia, M. & de Graef, M. Vector field electron tomography of magnetic materials: theoretical development. *Ultramicroscopy* **108**, 503–513 (2008).
104. Lai, G. M. *et al.* 3-dimensional reconstruction of magnetic vector-fields using electron-holographic interferometry. *J. Appl. Phys.* **75**, 4593–4598 (1994).
105. Lade, S. J., Paganin, D. & Morgan, M. J. Electron tomography of electromagnetic fields, potentials and sources. *Opt. Commun.* **253**, 392–400 (2005).

Acknowledgements

We are grateful to many colleagues for contributions to the work presented here, including M. Weyland, I. Arslan, T. J. V. Yates, M. H. Gass, E. P. W. Ward, L. Laffont, K. Kaneko, J. S. Barnard, J. Sharp, J. R. Tong, J.-C. Hernandez, A. Hungria, J. M. Thomas, T. Kasama, A. C. Twitchett-Harrison, R. J. Harrison, M. Pósfai and M. R. McCartney. Financial support from the European Union Framework 6 programme under a contract for an Integrated Infrastructure Initiative (Reference 026019 ESTEEM) is acknowledged. We are also grateful to the EPSRC, the Royal Society and RIKEN for financial support.